COMPARATIVE STUDY OF THE DESCRIPTIVE EXPERIMENT DESIGN AND ROBUST FUSED BAYESIAN REGULARIZATION TECHNIQUES FOR HIGH-RESOLUTION RADAR IMAGING

Ivan E. Villalon-Turrubiates, *Member*, *IEEE*, and Yuriy V. Shkvarko, *Senior Member, IEEE*

***Abstract*—In this paper, we perform a comparative study of two recently proposed high-resolution radar imaging paradigms: the descriptive experiment design regularization (DEDR) and the fused Bayesian regularization (FBR) methods. The first one, the DEDR, employs aggregation of the descriptive regularization and worst-case statistical performance (WCSP) optimization approaches to enhanced radar/SAR imaging. The second one, the FBR, performs image reconstruction as a solution of the ill-conditioned inverse spatial spectrum pattern (SSP) estimation problem with model uncertainties via unifying the Bayesian minimum risk (MR) estimation strategy with the maximum entropy (ME) randomized a priori image model and other projection-type regularization constraints imposed on the solution. Although the DEDR and the FBR are inferred from different descriptive and statistical constrained optimization paradigms, we examine how these two methods lead to structurally similar techniques that may be further transformed into new computationally more efficient robust adaptive imaging methods that enable one to derive efficient and consistent estimates of the SSP via unifying both the robust DEDR and FBR considerations. We present the results of extended comparative simulation study of the family of the image formation/ enhancement algorithms that employ the proposed robustified FBR and DEDR methods for high-resolution reconstruction of the SSP in a virtually real time. The computational complexity of different methods are analyzed and reported together with the scene imaging protocols. The advantages of the well designed SAR imaging experiments (that employ the FBR-based and DEDR-related robust estimators) over the cases of poorer designed experiments (that employ the conventional matched spatial filtering as well as the least squares techniques) are verified trough the simulation study.**

Index Terms—**Bayesian estimation, maximum entropy, radar imaging, regularization, remote sensing, spatial spectrum pattern, sufficient statistics.**

I. INTRODUCTION

THE goal of this study is to address and discuss a new computationally efficient approach to high-resolution radar/SAR imaging as an ill-conditioned inverse problem of estimating the spatial spectrum pattern (SSP) of the wavefield sources scattered from the probing surface (referred to as the radar/SAR image). The SSP estimation problem is a statistical ill-conditioned nonlinear inverse problem [6], [7]. Because of the stochastic nature and nonlinearity, no unique regular method exists for reconstructing the SSP from the finite-dimensional measurement data in an analytic closed form. Hence, the particular solution strategy to be developed and applied must unify the practical data observation method with some form of statistical regularization that incorporates the a priori model knowledge about the SSP to alleviate the problem ill-poseness. The classical imaging with radar or SAR implies application of the method called "matched spatial filtering" (MSF) that originates from the celebrated maximum likelihood (ML) estimation strategy [14]. In the statistical terms [2], [6], [14] such a method implies application of the adjoint SFO to the recorded data, computation of the squared norm of a filter outputs and their averaging over the actually recorded samples (the so-called snapshots [10]) of the independent data observations. As it was analyzed in many works, e.g. [1] – [27], the MSF method does not exploit all the "degrees of freedom" of the inverse problem at hand, thus manifests low spatial resolution performances. The recent non-parametric approaches to high-resolution enhanced radar/SAR imaging are based on treatment the problem at hand as an ill-posed (ill-conditioned) nonlinear inverse problem with model uncertainties [6] – [8], [15], [16]. The principal idea is to employ different regularization paradigms, e.g. [6] – [8] to resolve the SSP estimation inverse problem with minimum risk (i.e. maximum spatial resolution balanced with noise suppression) subject to some non-trivial ME and other projection-type constraints imposed on the solution (i.e. incorporate the a priori model information with minimum subjective decision making). In this study, we provide an overview of the recently developed descriptive experiment design regularization (DEDR) and the fused Bayesian

regularization (FBR) non-parametric paradigms for super-high-resolution radar/SAR image formation and enhancement/ reconstruction. The first one, the DEDR, developed in [26], [27] employs aggregation of the descriptive regularization and worst-case statistical performance (WCSP) optimization approaches to enhanced radar/SAR imaging. The second one, the FBR, developed in [7], [8], [25], performs image reconstruction as a solution of the ill-conditioned inverse spatial spectrum pattern (SSP) estimation problem with model uncertainties via unifying the Bayesian minimum risk (MR) estimation strategy with the maximum entropy (ME) randomized a priori image model that incorporates the projection-type regularization constraints imposed on the solution. Although the DEDR and the FBR are inferred from different descriptive and statistical constrained optimization paradigms, we examine how these two methods lead to structurally similar techniques that may be further transformed into new computationally more efficient robust adaptive imaging methods that enable one to derive efficient and consistent estimates of the SSP via unifying both the robust DEDR and FBR considerations. The principal innovative contribution of this study may be briefly summarized as follows:

- Unification of the family of the DEDR-related and FBR-related enhanced RS imaging techniques via comparative analysis of their operational computational structures.
- Development of the robustified versions of the DEDR and FBR methods via alleviating the ill-poseness of the nonlinear adaptive operator inversions in the overall image reconstruction procedures.
- Design of efficient computational algorithms that perform robust adaptive spatial processing for enhanced RS image formation in a virtually real computational time.

Also, we are going to present the results of extended comparative simulation studies of the family of the robustified DEDR-related and FBR-related SSP estimation algorithms using the MATLAB as simulation tools that provide efficiency and flexibility in performing all simulation experiments.

II. PROBLEM MODEL AND EXPERIMENT DESIGN CONSIDERATIONS

Consider a remote sensing experiment performed with a coherent array imaging radar or SAR (radar/SAR) that is traditionally referred to as radar imaging (RI) problem ([6] – [9]). The measurement sensor/SAR data wavefield $u(\mathbf{y}) = s(\mathbf{y}) + n(\mathbf{y})$ modeled as a superposition of the echo signals s and additive noise n is assumed to be available for observations and recordings within the prescribed time-space observation domain $Y \ni \mathbf{y}$, where $\mathbf{y} = (t, \mathbf{p})^{\mathrm{T}}$ defines the time-space points in the observation domain $Y = T \times P$.

A. RS motivated problem model

The model of the observation wavefield u is specified by the linear stochastic equation of observation (EO) of operator form:

$$u = Se + n; \quad e \in \mathrm{E}; \quad u, n \in \mathrm{U}; \; S: \mathrm{E} \to \mathrm{U} \tag{1}$$

on the Hilbert signal spaces E and U with the metric structures induced by the inner products,

$$[e_1, e_2]_{\mathrm{E}} = \int_X e_1(\mathbf{x}) e_2^*(\mathbf{x}) d\mathbf{x} \quad \text{and} \quad [u_1, u_2]_{\mathrm{U}} = \int_Y u_1(\mathbf{y}) u_2^*(\mathbf{y}) d\mathbf{y}\,, \tag{2}$$

respectively, where asterisk stands for complex conjugate. In (1), the S is referred to as the regular signal formation operator (SFO). It defines the transform of random scattered signals $e(\mathbf{x}) \in \mathrm{E}(X)$ distributed over the remotely sensed scene (probing surface) $X \ni \mathbf{x}$ into the echo signals $(Se(\mathbf{x}))(\mathbf{y}) \in \mathrm{U}(Y)$ over the time-space observation domain $Y = T \times P$; $t \in T$, $\mathbf{p} \in P$. In the functional terms [6], [9], such a transform is referred to as the operator S: E→U that maps the scene signal space E (the space of the signals scattered from the remotely sensed scene) onto the observation data signal space U. This operator model (1) in the conventional integral form [6] may be rewritten as

$$u(\mathbf{y}) = \int_X S(\mathbf{y}, \mathbf{x})\, e(\mathbf{x})\, d\mathbf{x} + n(\mathbf{y})\,, \tag{3}$$

$$e(\mathbf{x}) = e(f; \boldsymbol{\rho}, \boldsymbol{\theta}) = \int_F e\left(t; \boldsymbol{\rho}, \boldsymbol{\theta}\right) \exp\left(-\mathrm{i}2\pi f t\right) dt \tag{4}$$

where the functional kernel $S(\mathbf{y}, \mathbf{x})$ of the SFO S given by (1) defines the signal wavefield formation model [9], [11]. Following the multi-scale array/SAR radar RS problem phenomenology [6], [9], we adopt here an incoherent model of the backscattered field $e(\mathbf{x})$ in the frequency-space observation domain $X = F \times R = F \times P \times \Theta$, i.e. over the slant range $\boldsymbol{\rho} \in P$ and azimuth angle $\boldsymbol{\theta} \in \Theta$ domains, respectively. When tackling the RS spatial analysis problems, the radar engineers typically work in the frequency-space domain, $\mathbf{x} = (f; \boldsymbol{\rho}, \boldsymbol{\theta})^{\mathrm{T}} \in X = F \times P \times \Theta$ [6], [7], [9]. However, because of the one-to-one mapping, only the spatial cross range coordinates $\mathbf{r} = (\boldsymbol{\rho}, \boldsymbol{\theta})$ may be associated with $\mathbf{x} = \mathbf{r}$ as well [9], [11]. Such interpretation is valid if one assumes the narrowband system model [9], [11], [12] and incoherent nature of the backscattered field $e(\mathbf{x})$.

It is naturally inherent to the RS imaging experiments [7], [8], [11] to consider the phasor $e(f,\mathbf{r})$ in (3) to be an independent random variable at each frequency f, and spatial coordinates $\mathbf{r}$, $\boldsymbol{\theta}$ with the zero mean value and δ-form correlation function, $R_e(f, f'; \mathbf{r}, \mathbf{r}') = \langle e(f; \mathbf{r}) e^*(f', \mathbf{r}') \rangle = B(f, \mathbf{r}) \delta(f - f') \delta(\mathbf{r} - \mathbf{r}')$ that enables one to introduce the following definition of the spatial spectrum pattern (SSP) of the wavefield sources distributed in the RS observation environment [9], [27]

$$B(\mathbf{r}) = Aver^{(2)}\{e(\mathbf{r})\} = \int_F \left\langle |e(f, \mathbf{r})|^2 \right\rangle |H(f)|^2 df; \; \mathbf{r} \in R. \tag{5}$$

Here, <·> represents the ensemble averaging operator, while $Aver^{(2)}$ is referred to as the second order (i.e. nonlinear) statistical averaging operator defined by (5). Also in (5), $H(f)$ represents the given transfer function of the radar receive channels that we assume to be identical for all antenna array elements and impose the conventional normalization, $|H(f)|^2 = 1$ for all frequencies $f \in F$ in the radar receiver frequency integrating band F [9]. In the conventional radar imaging setting [9], [18], [21], the initial RS imaging problem is to form an estimate $\hat{B}(\mathbf{x})$ of the SSP distribution $B(\mathbf{r})$ over the remotely sensed scene $R \ni \mathbf{r}$ by processing whatever values of measurements of the data field, $u(\mathbf{y})$; $\mathbf{y} \in Y$, are available.

Next, following the RS data analysis methodology [1], [2], [20], [22] any particular physical signature of interest $\hat{\Lambda}(\mathbf{x})$ could be extracted from the reconstructed RS image $\hat{B}(\mathbf{x})$ applying the so-called deterministic *signature extraction operator* Λ. Hence, the particular RS signature (RSS) is mapped applying Λ to the reconstructed image, i.e.

$$\hat{\Lambda}(\mathbf{x}) = \Lambda(\hat{B}(\mathbf{x})). \tag{6}$$

Last, taking into account the RSS extraction model (6), we can reformulate now the RSS reconstruction problem as follows: to map the reconstructed particular RSS of interest $\hat{\Lambda}(\mathbf{x}) = \Lambda(\hat{B}(\mathbf{x}))$ over the observation scene $X \ni \mathbf{x}$ via post-processing whatever available values of the reconstructed scene image $\hat{B}(\mathbf{x})$; $\mathbf{x} \in X$.

B. Numerical model of the problem

Viewing it as an approximation problem leads one to the projection concept for a transformation of the continuous data field $u(\mathbf{y})$ to the $M \times 1$ vector $\mathbf{U} = (U_1, \ldots, U_M)^{\mathrm{T}}$ of sampled spatial-temporal data recordings. The M-d observations in the terms of projections [7], [8] can be expressed as

$$u_{(M)}(\mathbf{y}) = (P_{\mathrm{U}(M)}u)(\mathbf{y}) = \sum\nolimits_{m=1}^{M} U_m \varphi_m(\mathbf{y}) \tag{7}$$

with coefficients $\{U_m = [u, h_m]_{\mathrm{U}}\}$ where $P_{\mathrm{U}(M)}$ represents a projector onto the M-d subspace

$$\mathrm{U}_{(M)} = P_{\mathrm{U}(M)}\mathrm{U} = \mathrm{Span}\{\phi_m(\mathbf{y})\} \tag{8}$$

uniquely defined by a set of the orthogonal functions $\{\phi_m(\mathbf{y}) = \|h_m(\mathbf{y})\|^{-2} h_m(\mathbf{y});\ m = 1, \ldots, M\}$ that are related to $\{h_m(\mathbf{y})\}$ as a dual basis in $\mathrm{U}_{(M)}$ i.e. $[h_m, \phi_n]_{\mathrm{U}} = \delta_{mn}\ \forall\ m, n = 1, \ldots, M$. In the observation scene $X \ni \mathbf{x}$, the discretization of the scattering field $e(\mathbf{x})$ is traditionally performed over a $Q \times N$ rectangular grid where Q defines the dimension of the grid over the horizontal (azimuth) coordinate x_1 and N defines the grid dimension over the orthogonal coordinate x_2 (the number of the range gates projected onto the scene). The discretized complex scattering function is represented by coefficients [7], [8] $E_k = \mathrm{E}_{(q,n)} = [e, g_k]_{\mathrm{E}} = \int_X e(\mathbf{x}) g_k(\mathbf{x}) d\mathbf{x}$; $k = 1, \ldots, K = Q \times N$, of it decomposition over the grid composed of such identical shifted rectangular functions $\{g_k(\mathbf{x}) = g_{(q,n)}(\mathbf{x}) = 1$ if $\mathbf{x} \in \rho_{(q,n)}(\mathbf{x}) = \mathrm{rect}_{(q,n)}(x_1, x_2)$ and $g_k(\mathbf{x}) = 0$ for other $\mathbf{x} \notin \rho_{(q,n)}(\mathbf{x})$ for all $q = 1, \ldots, Q$; $n = 1, \ldots, N$; $k = 1, \ldots, K = Q \times N\}$. Hence, the K-d approximation of the scattering field becomes

$$e_{(K)}(\mathbf{x}) = (P_{\mathrm{E}(K)}e)(\mathbf{x}) = \sum\nolimits_{k=1}^{K} E_k g_k(\mathbf{x}) \tag{9}$$

where $P_{\mathrm{E}(K)}$ represents a projector onto such K-d signal approximation subspace

$$\mathrm{E}_{(K)} = P_{\mathrm{E}(K)}\mathrm{E} = \mathrm{Span}\{g_k(\mathbf{x})\} \tag{10}$$

spanned by K orthogonal grid functions (pixels) $\{g_k(\mathbf{x})\}$. Using such approximations, it is possible to proceed from the operator form (4) to its conventional numerical (vector) form

$$\mathbf{U} = \mathbf{S}\,\mathbf{E} + \mathbf{N}, \tag{11}$$

where $\mathbf{U}$, $\mathbf{N}$ and $\mathbf{E}$ define the vectors composed of the coefficients U_m, N_m and E_k of the finite-dimensional approximations of the fields u, n and e, respectively, and $\mathbf{S}$ is the matrix-form representation of the SFO with elements $\{S_{mk} = [Sg_k, h_m]_{\mathrm{U}} = \int_Y (Sg_k(\mathbf{x}))(\mathbf{y}) h_m^*(\mathbf{y}) d\mathbf{y}$; $k = 1, \ldots, K$; $m = 1, \ldots, M\}$ [6]. Zero-mean Gaussian vectors $\mathbf{E}$, $\mathbf{N}$ and $\mathbf{U}$ in (11) are characterized by the correlation matrices, $\mathbf{R}_{\mathbf{E}}$, $\mathbf{R}_{\mathbf{N}}$ and $\mathbf{R}_{\mathbf{U}} = \mathbf{S}\mathbf{R}_{\mathbf{E}}\mathbf{S}^{+} + \mathbf{R}_{\mathbf{N}}$, respectively, where superscript + defines the Hermitian conjugate when it stands with a matrix or a vector. Because of the incoherent nature of the scattering field $e(\mathbf{x})$, the vector $\mathbf{E}$ has a diagonal correlation matrix, $\mathbf{R}_{\mathbf{E}} = \mathrm{diag}(\mathbf{B}) = \mathbf{D}(\mathbf{B})$, in which the $K \times 1$ vector of the principal diagonal $\mathbf{B}$ is composed of elements $B_k = \langle E_k E_k^* \rangle$; $k = 1, \ldots, K$. This vector $\mathbf{B}$ is referred to as a vector-form representation of the SSP. Hence, using the definition (6) the K-d approximation of the desired RS signature estimate $\hat{\Lambda}_{(K)}(\mathbf{x})$ as a continuous function of $\mathbf{x} \in X$ over the probing scene X is now expressed as follows

$$\hat{\Lambda}_{(K)}(\mathbf{x}) = \mathrm{est}\{\Lambda \langle |e_{(K)}(\mathbf{x})|^2 \rangle\} = \sum\nolimits_{k=1}^{K} \Lambda(\hat{B}_k) g_k(\mathbf{x});\ \mathbf{x} \in X. \tag{12}$$

Analyzing (12), one may deduce that in every particular measurement scenario (specified by the corresponding approximation spaces $\mathrm{U}_{(M)}$ and $\mathrm{E}_{(K)}$) one has to derive the estimate $\hat{\mathbf{B}}$ of a vector-form approximation of the SSP that uniquely defines via (12) the approximated continuous pixel-format reconstructed map $\hat{\Lambda}_{(K)}(\mathbf{x})$ of the desired RS signature distributed over the observed scene $X \ni \mathbf{x}$. Hence, the vector

$$\hat{\mathbf{\Lambda}} = \mathrm{vec}\{\Lambda(\hat{B}_k);\ k = 1, \ldots, K\} \tag{13}$$

represents the numerical (i.e., vector-form) model of the reconstructed RS signature (RSS) in the conventional pixel format. Thus, the desired continuous-form RSS is uniquely

reconstructed from the estimate $\hat{\mathbf{B}}$ of the SSP vector (pixel-formatted image) via (12).

C. Experiment-design considerations

The experiment design (ED) aspects of the problem at hand implies the analysis of how to choose (finely adjust) the basis functions $\{g_k(\mathbf{r})\}$ that span the signal representation subspace $\mathrm{E}_{(K)} = P_{\mathrm{E}(K)}\mathrm{E} = \mathrm{Span}\{g_k\}$ for a given observation subspace $\mathrm{U}_{(M)} = \mathrm{Span}\{\varphi_m\}$ [6], [8], [12]. Here, we formalize such the ED considerations via imposing the metrics structure in the solution space [6], [8] defined by the inner product

$$\|\mathbf{B}\|^2_{\mathrm{B}(K)} = [\mathbf{B}, \mathbf{MB}] \tag{14}$$

where $\mathrm{B}(K)$ represents the so-called correctness convex solution set [6], and $\mathbf{M}$ is referred to as the metrics inducing operator. Hence, the selection of $\mathbf{M}$ provides additional geometrical ED degrees of freedom of the problem model. In this study, we specify the model for $\mathbf{M}$ that corresponds to the numerical approximation of the Tikhonov's stabilizer of the second order [6], [8]. Next, following [6], we incorporate the projection-type a priori information, in which case the SSP vector $\mathbf{B}$ satisfies the linear constraint equation

$$\mathbf{GB} = \mathbf{C}, \quad \text{i.e. } \mathbf{G}^{-}\mathbf{GB} = \mathbf{B}_P \tag{15}$$

where $\mathbf{B}_P = \mathbf{G}^{-}\mathbf{C}$ and $\mathbf{G}^{-}$ is the Moore-Penrose pseudoinverse of a given projection constraint operator $\mathbf{G}$: $\mathrm{B}_{(K)} \to \mathrm{B}_{(Q)}$, and the constraint vector $\mathbf{C} \in \mathrm{B}_{(Q)}$ and the constraint subspace $\mathrm{B}_{(Q)}$ ($Q < K$) are assumed to be given [8]. In (15), the constraint operator $\mathbf{G}$ projects the portion of the unknown SSP onto the subspace where the SSP values are fixed by $\mathbf{C}$. In practice, such limitations may specify also the system calibration [15], [22].

III. HIGH-RESOLUTION NONPARAMETRIC IMAGING

A. DEDR method

In the descriptive statistical formalism, the desired SSP vector $\hat{\mathbf{B}}$ is recognized to be the vector of the principal diagonal of an estimate of the correlation matrix $\mathbf{R}_{\mathbf{E}}(\mathbf{B})$, i.e. $\hat{\mathbf{B}} = \{\hat{\mathbf{R}}_{\mathbf{E}}\}_{\mathrm{diag}}$. Thus, one can seek to estimate $\hat{\mathbf{B}} = \{\hat{\mathbf{R}}_{\mathbf{E}}\}_{\mathrm{diag}}$ given the data correlation matrix $\mathbf{R}_{\mathbf{U}}$ pre-estimated via averaging $J \geq 1$ independent sampled correlations [1], [24]

$$\hat{\mathbf{R}}_{\mathbf{U}} = \mathbf{Y} = \underset{j \in J}{\mathrm{aver}} \{\mathbf{U}_{(j)}\mathbf{U}^{+}_{(j)}\} = \frac{1}{J}\sum\nolimits_{j=1}^{J} \mathbf{U}_{(j)}\mathbf{U}^{+}_{(j)}, \tag{16}$$

and determining the solution operator (SO) $\mathbf{F}$ such that

$$\hat{\mathbf{B}} = \{\hat{\mathbf{R}}_{\mathbf{E}}\}_{\mathrm{diag}} = \{\mathbf{FYF}^{+}\}_{\mathrm{diag}}. \tag{17}$$

To optimize the search for the desired SO $\mathbf{F}$ we reformulate here the *DEDR* strategy [26], [27]

$$\mathbf{F} = \arg\min_{\mathbf{F}}\{\mathcal{R}(\mathbf{F})\} \quad \text{subject to} \quad <\|\boldsymbol{\Delta}\|^2>_{p(\boldsymbol{\Delta})} \leq \delta \tag{18}$$

where the conditioning term represents the statistical worst-case statistical performance (WCSP) regularization constraint imposed on the unknown particular disturbed component of the uncertain SFO matrix [26], $\tilde{\mathbf{S}} = \mathbf{S} + \boldsymbol{\Delta}$, where $\mathbf{S}$ represents the regular SFO, $\boldsymbol{\Delta}$ represents the random SFO perturbation term, and the DEDR "augmented risk" functional is defined as

$$\mathcal{R}(\mathbf{F}) = \mathrm{tr}\{<(\mathbf{F}\tilde{\mathbf{S}} - \mathbf{I})\mathbf{A}(\mathbf{F}\tilde{\mathbf{S}} - \mathbf{I})^{+}>_{p(\boldsymbol{\Delta})}\} + \alpha\,\mathrm{tr}\{\mathbf{FR_NF}^{+}\}. \tag{19}$$

The DEDR strategy (18) implies the minimization of the weighted sum of the systematic and fluctuation errors (19) in the desired estimate (17), in which the unknown disturbances of the SFO $\boldsymbol{\Delta}$ are treated through the WCSP bounding constraint (18) imposed onto the averaged squared norm of $\boldsymbol{\Delta}$. The selection (adjustment) of the regularization parameter α and the weight matrix $\mathbf{A}$ provides the additional DEDR "degrees of freedom" incorporating any descriptive properties of a solution if those are known a priori [26], [27]. We incorporate also two additional requirements into such DEDR strategy: (i) the SO must involve the adjoint SFO $\mathbf{S}^{+}$ (to satisfy the observability condition [26]); (ii) the resulting SO must admit a representation form that does *not* involve the inversion of $\mathbf{Y}$ (to be applicable to the scenarios with the low-rank $\mathbf{Y}$, e.g. SAR imaging). These additional requirements constitute the principal distinguishing aspects of the pursued DEDR approach from the conventional minimum risk strategies [9], [14], [24] and lead to the following reformulated conditional optimization problem [26], [27]

$$\mathbf{F} = \arg\min_{\mathbf{F}} \max_{<\|\Delta\|^2>_{p(\Delta)} \leq \delta} \{\mathcal{R}(\mathbf{F})\}. \tag{20}$$

To proceed with the derivation of the SO (20), in [26], [27] the following was performed: (i) decomposition of risk (19); (ii) evaluation of the maximum value β of the bounding constraint in (20) applying the Cauchy-Schwarz inequality. Doing this, we translate the original min-max problem (20) into the equivalent (under the specified constraints) aggregated optimization problem

$$\mathbf{F} = \arg\min_{\mathbf{F}}\{\mathcal{R}_{DEDR}(\mathbf{F})\} \tag{21}$$

with the aggregated DEDR risk functional,

$$\mathcal{R}_{DEDR}(\mathbf{F})\} = \mathrm{tr}\{(\mathbf{FS} - \mathbf{I})\mathbf{A}(\mathbf{FS} - \mathbf{I})^{+}\} + \alpha\,\mathrm{tr}\{\mathbf{F}\,\mathbf{R}_{\Sigma}\,\mathbf{F}^{+}\} \tag{22}$$

where

$$\mathbf{R}_{\Sigma} = \mathbf{R}_{\Sigma}(\beta) = (\mathbf{R_N} + \beta\,\mathbf{I}); \ \beta = \delta/\alpha \geq 0. \tag{23}$$

The solution of the minimization problem (21) was derived and detailed in [26], [27]; the resulting SO has the following representation

$$\mathbf{F}_{DEDR} = \mathbf{K}_{\mathbf{A},\alpha,\beta}\mathbf{S}^{+}\mathbf{R}_{\Sigma}^{-1} \tag{24}$$

i.e., is a composition of the whitening filter, $\mathbf{R}_{\Sigma}^{-1}$, the matched spatial filter, $\mathbf{S}^{+}$, and the regularized reconstruction operator

$$\mathbf{K}_{\mathbf{A},\alpha,\beta} = (\mathbf{S}^{+}\mathbf{R}_{\Sigma}^{-1}\mathbf{S} + \alpha\mathbf{A}^{-1})^{-1}. \tag{25}$$

Note that the derived SO (24) involves $\mathbf{S}^{+}$ (i.e. satisfies the DED-observability constraints) and does not involve the inversion of $\mathbf{Y}$ (i.e. is applicable to reconstructive SAR imaging problems with only one recorded realization of the trajectory data signal available for further processing, $J = 1$).

B. FBR method

The robustified numerical version of the fused Bayesian-regularization (FBR) method for reconstruction of the power spatial spectrum pattern (SSP) of the wave field scattered from a remotely sensing scene (that is referred to as a desired RS image) given a finite set of array radar/SAR signal recordings was developed originally in [7]. Since the SSP estimation is in essence a nonlinear numerical inverse problem, the proposition in [7], [8] was to alleviate the problem ill-poseness by robustification of the Bayesian estimation strategy [14], [24] via performing the non adaptive approximations of the reconstructive operators that incorporate the non trivial metrics considerations for designing the proper solution space and different regularization constraints imposed on a solution.

The estimator that produces the high-resolution optimal (in the sense of the Bayesian minimum risk strategy) estimate $\hat{\mathbf{B}}$ of the SSP vector via processing the M-d data recordings $\mathbf{U}$ applying the FBR estimation strategy that incorporates also nontrivial a priori geometrical and projection-type model information was developed in [7] and [8]. Such optimal FBR estimate of the SSP is given by the nonlinear equation

$$\hat{\mathbf{B}} = \mathbf{B}_{P} + \mathbf{P}\mathbf{B}_{0} + \mathbf{W}(\hat{\mathbf{B}})\{\mathbf{V}(\hat{\mathbf{B}}) - \mathbf{Z}(\hat{\mathbf{B}})\}. \tag{26}$$

In (26), the constraint $\mathbf{B}_{P}$ is specified by (15) and $\mathbf{B}_{0}$ represents the a priori SSP distribution to be considered as a zero step approximation to the desires SSP estimate $\hat{\mathbf{B}}$. The sufficient statistics (SS) vector $\mathbf{V}(\hat{\mathbf{B}}) = \{\mathbf{F}(\hat{\mathbf{B}})\mathbf{U}\mathbf{U}^{+}\mathbf{F}^{+}(\hat{\mathbf{B}})\}_{\mathrm{diag}}$ (vector composed of the principal diagonal of the embraced matrix) is formed via applying to the measured data vector $\mathbf{U}$, the solution-dependent SS formation operator [7]

$$\mathbf{F} = \mathbf{F}(\hat{\mathbf{B}}) = \mathbf{D}(\hat{\mathbf{B}})(\mathbf{I} + \mathbf{S}^{+}\mathbf{R}_{\mathbf{N}}^{-1}\mathbf{S}\mathbf{D}(\hat{\mathbf{B}}))^{-1}\mathbf{S}^{+}\mathbf{R}_{\mathbf{N}}^{-1}. \tag{27}$$

The SS shift vector in (26) is defined as $\mathbf{Z}(\hat{\mathbf{B}})$ [7], and the composite solution-dependent smoothing-projection window operator

$$\mathbf{W}(\hat{\mathbf{B}}) = \mathbf{P}_{\mathbf{W}}\boldsymbol{\Omega}(\hat{\mathbf{B}}) \tag{28}$$

is composed of the projector

$$\mathbf{P}_{\mathbf{W}} = (\mathbf{I} - \mathbf{G}^{-}\mathbf{G}) \tag{29}$$

and the solution dependent smoothing window

$$\boldsymbol{\Omega}(\hat{\mathbf{B}}) = [\mathrm{diag}(\{\mathbf{S}^{+}\mathbf{F}^{+}\mathbf{F}\mathbf{S}\}_{\mathrm{diag}}) + \hat{\alpha}\,\mathbf{D}^{2}(\hat{\mathbf{B}})\mathbf{M}(\hat{\mathbf{B}})]^{-1}, \tag{30}$$

in which the regularization parameter $\hat{\alpha}$ is to be adaptively adjusted using the system calibration data [7], [8]. The resulting FBR-optimal estimate in the numerical (discrete pixel) format is given by

$$\hat{\mathbf{B}}_{FBR} = \mathbf{B}_{P} + \mathbf{P}\mathbf{B}_{0} + \mathbf{W}(\hat{\mathbf{B}})\{\mathbf{V}(\hat{\mathbf{B}}) - \mathbf{Z}(\hat{\mathbf{B}})\}. \tag{31}$$

Because of the non-linearity and complexity of the solution-dependent K-d operator inversions needed to be performed to compute the SS $\mathbf{V}(\hat{\mathbf{B}})$, the window $\mathbf{W}(\hat{\mathbf{B}})$ and SS shift $\mathbf{Z}(\hat{\mathbf{B}})$, the computational load of such optimal FBR estimator (26), (31) developed originally in [7], [8] is extremely high to address that as a practically realizable estimator of the SSP and RSS (i.e. practical high-resolution RS radar imaging and signature mapping technique realizable to operate in a real-time mode).

C. DEDR-related and FBR-related robust spatial filtering (RSF) techniques

The robustification scheme for real-time implementation of the DEDR estimator (17) and the FBR estimator (26), (31) enables one to reduce drastically the computation load of the image formation procedure without substantial degradation in the resolution and overall image performances. Here first, we propose the robustified versions of the DEDR estimator defined by (17) and the FBR estimator given by (26) that we refer to as the robust FBR reconstructive filtering (RFBR) method. This method is a direct generalization of the previous one proposed in [7] and [8] that we perform here via roughing $\mathbf{P}_{\mathbf{W}} = \mathbf{I}$ and approximating both the SS formation operator $\mathbf{F}(\hat{\mathbf{B}})$ and the smoothing window $\boldsymbol{\Omega}(\hat{\mathbf{B}})$ in (26) by roughing $\mathbf{D}(\hat{\mathbf{B}}) \approx \mathbf{D} = b_0\mathbf{I}$, where b_0 represents the expected a priori image grey level [7], [8]. Hence, the robustified SS formation operator

$$\mathbf{F} = \mathbf{A}^{-1}(\rho)\mathbf{S}^{+} \quad \text{with} \quad \mathbf{A}(\rho) = \mathbf{S}^{+}\mathbf{S} + \rho^{-1}\mathbf{I} \tag{32}$$

becomes the regularized inverse of the SFO $\mathbf{S}$ with regularization parameter ρ^{-1}, the inverse of the signal-to-noise ratio (SNR) $\rho = b_0/N_0$ for the adopted white observation noise model, $\mathbf{R}_{\mathbf{N}} = N_0\mathbf{I}$ with intensity N_0. In that case, the robust smoothing window

$$\mathbf{W} = \boldsymbol{\Omega} = (w_0\mathbf{I} + \mathbf{M})^{-1} \tag{33}$$

is completely defined by the matrix $\mathbf{M}$ that induces the metrics structure in the solution space [6] with the scaling factor $w_0 = \mathrm{tr}\{\mathbf{S}^{+}\mathbf{F}^{+}\mathbf{F}\mathbf{S}\}/K$. Such robustified $\mathbf{W}$ can be pre-computed a

priori for a family of different admissible ρ as it was proposed in the previous studies [7], [8]. Here, we employ a practical constraints of high SNR operational conditions [22], ρ >> 1, in which case one can neglect also the constant bias $\mathbf{Z} = Z_0\mathbf{I}$ in (26) because it does not affect the pattern of the SSP estimate (it influences only the constant grey level in the resulting solution but $Z_0 << \beta$ for ρ >> 1). Following these practically motivated assumptions, the resulting RFBR estimator for the SSP becomes

$$\hat{\mathbf{B}}_{RFBR} = \mathbf{B}_0 + \mathbf{\Omega V}\,, \tag{34}$$

where $\mathbf{V} = \{\mathbf{FUU}^{+}\mathbf{F}^{+}\}_{\text{diag}}$ represents now the robust SS vector.

D. Matched spatial filtering (MSF) algorithm

The simplest rough SSP and RSS estimators can be constructed as further simplification of (34) if the trivial a priori model information ($\mathbf{P_W} = \mathbf{I}$ and $\mathbf{B}_0 = b_0\mathbf{I}$) is adopted, and roughly approximate the SS formation operator **F** by the adjoint SFO, i.e. the matched filter

$$\mathbf{F} \approx \gamma_0\mathbf{S}^{+} \tag{35}$$

where the normalizing constant γ_0 provides balance of the operator norms $\gamma_0^2 = \text{tr}^{-1}\{\mathbf{S}^{+}\mathbf{SS}^{+}\mathbf{S}\}\text{tr}\{\mathbf{FSS}^{+}\mathbf{F}^{+}\}$ [6]. In that case, the estimator (34) is simplified to its rough matched spatial filter (MSF) version

$$\hat{\mathbf{B}}_{MSF} = \mathbf{\Omega\Pi}\,, \tag{36}$$

where the rough SS, $\mathbf{\Pi} = \gamma_0^2\{\mathbf{S}^{+}\mathbf{UU}^{+}\mathbf{S}\}_{\text{diag}}$, is now formed applying the adjoint operator (i.e. the matched spatial filter) $\mathbf{S}^{+}$, and the windowing of the rough SS **Π** is performed applying the smoothing filter $\mathbf{\Omega} = (w_0\mathbf{I} + \mathbf{M})^{-1}$ with the nonnegative entry [7], [8]. The (36) is referred to as matched spatial filtering (MSF) algorithm for estimation of the SSP. Equation (36) is recognized to be a vector-form representation of the conventional kernel SSP estimation algorithm [9], [24], in which the SS is formed as the squared modulus of the outcomes of the matched spatial filter applied to the recorded data signal (trajectory signal in the SAR terminology [12], [23]). Thus, in the framework of the FBR inference-based approach to RS imaging [6], the traditional MSF technique (36) can be viewed as a rough simplified version of the RFBR algorithm (34).

E. Robust adaptive spatial filtering (RASF) algorithm

The RASF solution operator (SO) is a modification of the (27) for the case of an arbitrary zero-mean noise with the correlation matrix $\mathbf{R_N}$, the equal importance of the systematic and noise error measures, i.e. $\alpha = 1$, and the solution dependent weight matrix $\mathbf{A} = \hat{\mathbf{D}}^{-1}$. In this case, the SO is recognized to be the robust adaptive spatial filter (RASF)

$$\mathbf{F}_{RASF} = (\mathbf{S}^{+}\mathbf{R}_{\mathbf{N}}^{-1}\mathbf{S} + \hat{\mathbf{D}}^{-1})^{-1}\mathbf{S}^{+}\mathbf{R}_{\mathbf{N}}^{-1}\,. \tag{37}$$

IV. QUALITY METRICS

The traditional quantitative quality metric [1] for RS images is the so-called Improvement in the Output Signal to Noise Ratio (IOSNR), which provides the metrics for performance gains attained with different employed estimators in dB scale

$$IOSNR(dB) = 10\cdot\log_{10}\left(\frac{\sum_{k=1}^{K}\left(\hat{b}_k^{(MSF)} - b_k\right)^2}{\sum_{k=1}^{K}\left(\hat{b}_k^{(p)} - b_k\right)^2}\right), \quad p = 1,...,P\,, \tag{38}$$

where b_k represents the value of the k-th element (pixel) of the original SSP, $\hat{b}_k^{(MSF)}$ represents the value of the k-th element (pixel) of the rough SSP estimate formed applying the matched spatial filtering (MSF) method, and $\hat{b}_k^{(p)}$ represents the value of the k-th element (pixel) of the enhanced SSP estimate formed applying the pth enhanced imaging method ($p = 1,\ldots,P$), respectively.

The percentage IOSNR (PIOSNR) quality metric is a modification of the IOSNR metric [22]; it expresses the percentage of the gained reconstruction improvement specified as follows

$$PIOSNR(\%) = 100\left(1 - \frac{\sum_{k=1}^{K}\left(\hat{b}_k^{(p)} - b_k\right)^2}{\sum_{k=1}^{K}\left(\hat{b}_k^{(MSF)} - b_k\right)^2}\right), \quad p = 1,...,P\,. \tag{39}$$

Finally, the total Mean Square Error (MSE) is a quality metric defined as [24]

$$MSE = \sum_{k=1}^{K}\left(\hat{b}_k^{(p)} - b_k\right)^2\,, \quad p = 1,...,P\,. \tag{40}$$

The quality metrics specified by (38), (39) and (40) allow to quantify the performances of the employed SSP and RSS reconstructive estimation methods (enumerated by $p = 1,\ldots,P$).

V. SIMULATIONS

The first simulation experiment was performed for the test (artificially synthesized) scenes imaging applying the SAR with partially synthesized aperture as an RS imaging system [8]. The SFO of all RS images were factorized along two axes in the image plane: the azimuth (horizontal axis, x_1) and the range (vertical axis, x_2). Following the common practically motivated technical considerations [5], [12], [23] we modelled a triangular shape of the SAR range ambiguity function (AF) $\Psi_r(x_2)$ in the x_2 direction, and a $|sinc|^2$ shape of the side-looking SAR azimuth AF $\Psi_a(x_1)$ in the x_1 direction at the zero crossing level for the simulated SAR system with fractionally synthesized array [8], [23], [24].

The behavior and performance indices of the described estimators were examined for five RS system configurations applied to three test scenes as specified below.

In the first simulation scenario, the assigned values of the AF widths were: 5 pixels width for $\Psi_r(x_2)$ and 10 pixels width for $\Psi_a(x_1)$. In the simulations reported in Fig. 1, we considered the case of white Gaussian observation noise with the SNR of 30 dB. Figure 1(a) shows the 512×512-pixel original synthesized test scene. Figure 1(b) reports the image formed implementing the MSF method. Figure 1(c) presents the reconstructed (enhanced) synthesized image formed using the RASF estimator. Figure 1(d) shows the reconstructed (enhanced) synthesized image formed using the DEDR estimator. Figure 1(e) presents the reconstructed (enhanced) synthesized image formed using the FBR estimator. Last, Figure 1(f) shows the reconstructed (enhanced) synthesized image formed using the RFBR estimator. The quantitative quality metrics of the *IOSNR*, *PIOSNR* and *MSE* gained with the employed enhanced imaging methods for the simulated fractional aperture synthesis scenarios with different levels of noise are reported in Table 1.

In the second simulation scenarios, the high-resolution real-world environmental images were used as test scenes [4]. The first tested scene is shown in Fig. 2(a) and the second tested scene is shown in Fig. 3(a). The simulation experiments were run with the following system-level specifications: 5 pixels width for $\Psi_r(x_2)$ and 20 pixels width for $\Psi_a(x_1)$, respectively. In the basic simulations, we considered the case of white Gaussian observation noise with the SNR of 30 dB. Figures 2(b) and 3(b) show the images formed via implementing the MSF method with the system parameters specified in the figure captions. Figures 2(c) and 3(c) present the reconstructed (enhanced) images formed using the RASF estimator. Figures 2(d) and 3(d) show the enhanced images reconstructed with the DEDR method. Figures 2(e) and 3(e) present the reconstructed (enhanced) images formed using the FBR estimator. Figures 2(f) and 3(f) show the enhanced images reconstructed with the RFBR method. The quantitative quality metrics of the *IOSNR*, *PIOSNR* and *MSE* gained with different tested enhanced imaging methods for the simulated fractional aperture synthesis scenarios with different levels of noise are reported in Tables 2 and 3, respectively.

In the third reported here simulation scenario that was run with the second real-world SAR scene, the system-level specifications were as follows: 5 pixels width for $\Psi_r(x_2)$, 40 pixels width for $\Psi_a(x_1)$ for the first (1^{st}) system and 50 pixels width for $\Psi_a(x_1)$ for the second (2^{nd}) simulated fractional SAR imaging system with SNR of 30 dB. Figures 4(a) and 5(a) show the 512×512-pixel high-resolution original scene. Figures 4(b) and 5(b) present the images of the same scene formed implementing the MSF method. Figures 4(c) and 5(c) display the reconstructed (enhanced) scene images formed using the RASF estimator. Figures 4(d) and 5(d) show the enhanced images reconstructed with the DEDR method. Figures 4(e) and 5(e) display the enhanced scene images reconstructed using the FBR estimator. Last, figures 4(f) and 5(f) present the reconstructed (enhanced) images formed using the RFBR technique. The *IOSNR*, *PIOSNR* and *MSE* quantitative quality metrics gained with different simulated enhanced imaging methods for different fractional SAR operational scenarios and different levels of noise are reported in Tables 4 and 5, respectively. The presented simulation protocols are indicative of improvements both in the qualitative and quantitative metrics gained with the proposed robust DEDR and FBR-related techniques in comparison with the conventional MSF and RSF algorithms.

VI. COMPUTATIONAL COMPLEXITY

Real-time computing is traditionally referred to as study of software systems which are subject to some real-time operational constraints [1] (e.g., operational deadlines from en event to a system response) [19]. By contrast, a non-real-time system is one for which there is no deadline, even if fast response or high performance is desired or preferred [1], [19]. The needs of real-time software are often addressed in the context of real-time operating systems [1], and synchronous programming languages [2], which provide frameworks on which to build up the real-time application software [2], [3].

A real time RS data processing/imaging system is one, which performances can be considered (within a particular RS context) to be mission critical [3]. Real-time computations can be said to have failed if they are not completed before their deadline, where the deadline is relative to an RS event [19]. A real-time deadline must be met, regardless of system load [1].

For the previously described image enhancement and SSP/RSS mapping methodologies, it is reasonable to define the computational complexity via determining the number of computational operations needed to perform the particular employed algorithms [10]. Consider $\boldsymbol{K}$ as a matrix, $\boldsymbol{I}$ as an inverse matrix. Let suffix n represents the number of matrix multiplications and/or inversions required to complete the mathematical operations (e.g., $\boldsymbol{K}^{(4)}$ represents a quadruple matrix multiplication, $\boldsymbol{I}^{(2)}$ represents a double matrix inversion, etc.). For the particular employed simulation formats, $\boldsymbol{K}$ and $\boldsymbol{I}$ are 512×512 matrixes. The number of operations needed to complete one reconstruction cycle for the tested and compared methods are reported in Table 6. With these results, one can analyze the processing time (in operation cycles) needed to perform computationally each proposed/employed algorithm. Last, Table 7 reports the computational times required for completing the compared SSP/RSS reconstructive techniques with three different typical computer processing unit (CPU) clock speeds: (i) with a personal computer (PC) running at 2.66 GHz with a single processor; (ii) with a workstation (WS) running at 3.80 GHz

with a duo processor, and (iii) with a dedicated hardware (DH) running at 300 MHz with a single processor.

The presented results of comparative simulation analysis illustrate the behavior and overall imaging performance improvements gained with the proposed robust DEDR and FBR-related approaches compared with other previously developed methods [1], [4], [12], [20] in both the reconstruction quality metrics and computational complexity reduction. The advantages of the well designed robust imaging experiments (that employ the RASF, DEDR, and RFBR methods) over the cases of poorer designed experiments (that employ the conventional MSF and RSF algorithms) were investigated through extensive simulation study and reported here for different multi-grade test scenes.

a. Original artificially synthesized test scene.

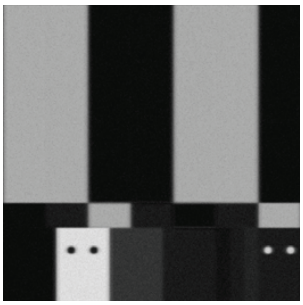

b. Low-resolution scene image formed applying the MSF method.

c. Test scene reconstruction using the RASF estimator.

d. Test scene reconstruction using the DEDR estimator.

e. Test scene reconstruction using the FBR estimator.

f. Test scene reconstruction using the robust RFBR estimator.

Fig. 1. Simulation results of the synthesized test scene SSP reconstruction. Specifications of the simulation experiment are summarized in Table 1.

a. First real-world original high-resolution scene.

b. Low-resolution scene image formed applying the MSF method.

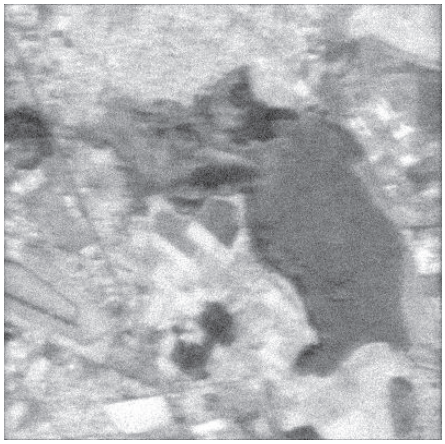

c. Scene reconstruction using the RASF estimator.

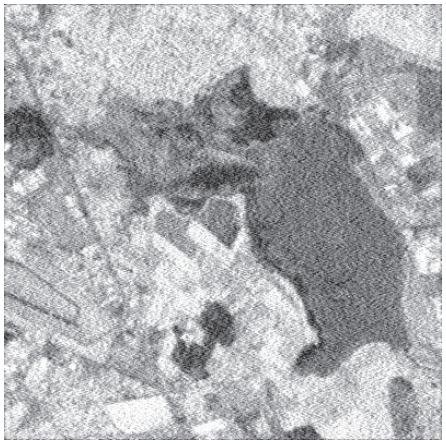

d. Scene reconstruction using the DEDR estimator.

e. Scene reconstruction using the FBR estimator.

f. Scene reconstruction using the robust RFBR estimator.

Fig. 2. Simulation results of the first real-world SAR scene imaging with SSP reconstruction performed with the 1st system.
Specifications of the simulation experiment are summarized in Table 2.

a First real-world original high-resolution scene.

b. Low-resolution scene image formed applying the MSF method.

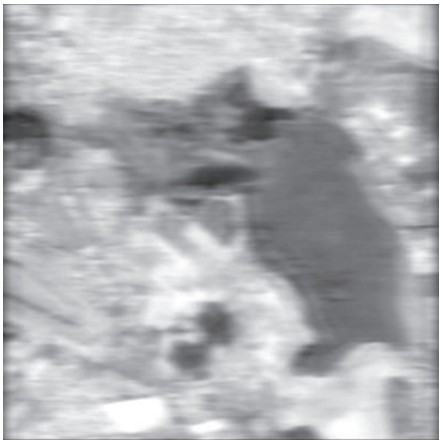

c. Scene reconstruction using the RASF estimator.

d. Scene reconstruction using the DEDR estimator.

e. Scene reconstruction using the FBR estimator.

f. Scene reconstruction using the robust RFBR estimator.

Fig. 3. Simulation results of the first real-world SAR scene imaging with SSP reconstruction performed with the 2nd system.
Specifications of the simulation experiment are summarized in Table 3.

a. Second real-world original high-resolution scene.

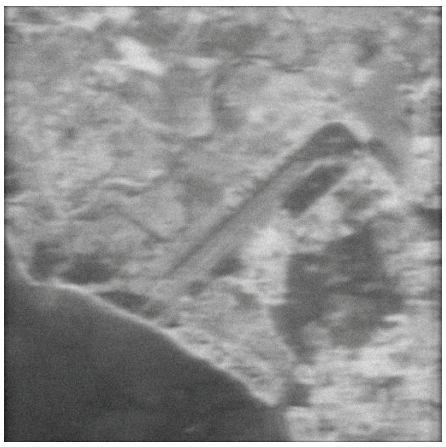

b. Low-resolution scene image formed applying the MSF method.

c. Scene reconstruction using the RASF estimator.

d. Scene reconstruction using the DEDR estimator.

e. Scene reconstruction using the FBR estimator.

f. Scene reconstruction using the robust RFBR estimator.

Fig. 4. Simulation results of the first real-world SAR scene imaging with SSP reconstruction performed with the 1st system.
Specifications of the simulation experiment are summarized in Table 4.

a. Second real-world original high-resolution scene.

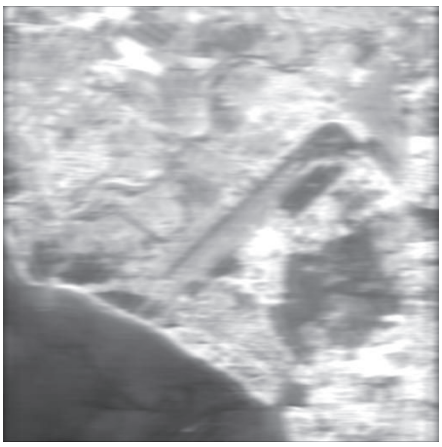

b. Low-resolution scene image formed applying the MSF method.

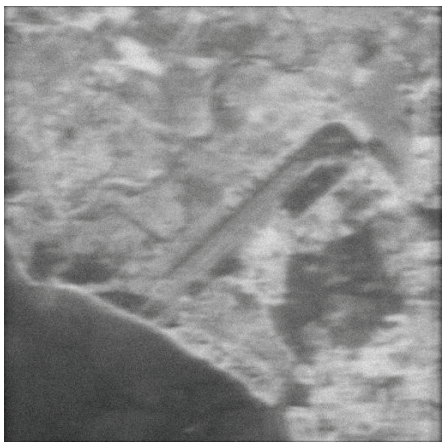

c. Scene reconstruction using the RASF estimator.

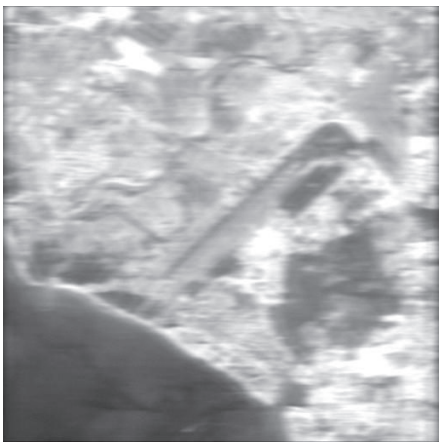

d. Scene reconstruction using the DEDR estimator.

e. Scene reconstruction using the FBR estimator.

f. Scene reconstruction using the robust RFBR estimator.

Fig. 5. Simulation results of the first real-world SAR scene imaging with SSP reconstruction performed with the 2nd system.
Specifications of the simulation experiment are summarized in Table 5.

TABLE 1

COMPARATIVE TABLE OF THE QUALITY METRICS GAINED WITH DIFFERENT ESTIMATION METHODS FOR THREE LEVELS OF NOISE (SNR).
RESULTS ARE REPORTED FOR THE SYNTHESIZED TEST SCENE.
SYSTEM SPECIFICATIONS: RANGE TRIANGULAR SHAPE OF AF $\Psi_R(X_2) = 5$ PIXELS WIDTH; AZIMUTH $|SINC|^2$ SHAPE OF AF $\Psi_A(X_1) = 10$ PIXELS WIDTH.

	Method →	**RASF**			**DEDR**			**FBR**			**RFBR**		
	SNR [dB] →	**20**	**25**	**30**	**20**	**25**	**30**	**20**	**25**	**30**	**20**	**25**	**30**
Metrics	**IOSNR [dB]**	15.65	20.84	25.23	13.54	18.85	23.45	10.26	14.76	17.37	11.16	15.53	18.36
	PIOSNR (%)	72.34	78.16	77.06	76.74	84.77	79.69	92.82	92.75	95.54	91.73	91.43	94.33
	MSF	0.20	0.50	0.60	0.23	0.40	0.50	0.03	0.20	0.10	0.04	0.22	0.14

TABLE 2

COMPARATIVE TABLE OF THE QUALITY METRICS GAINED WITH DIFFERENT ESTIMATION METHODS FOR THREE LEVELS OF NOISE (SNR).
RESULTS ARE REPORTED FOR THE 1ST SYSTEM APPLIED TO THE FIRST SAR SCENE.
SYSTEM SPECIFICATIONS: RANGE TRIANGULAR SHAPE OF AF $\Psi_R(X_2) = 5$ PIXELS WIDTH; AZIMUTH $|SINC|^2$ SHAPE OF AF $\Psi_A(X_1) = 20$ PIXELS WIDTH.

	Method →	**RASF**			**DEDR**			**FBR**			**RFBR**		
	SNR [dB] →	**15**	**20**	**25**	**15**	**20**	**25**	**15**	**20**	**25**	**15**	**20**	**25**
Metrics	**IOSNR [dB]**	10.15	15.32	20.25	8.76	13.74	18.84	5.47	9.85	12.63	6.15	10.62	13.04
	PIOSNR (%)	81.37	86.62	85.24	83.22	91.14	90.21	96.63	91.68	99.10	95.18	90.29	98.24
	MSF	0.16	0.46	0.57	0.18	0.37	0.46	0.02	0.24	0.24	0.03	0.29	0.34

TABLE 3

COMPARATIVE TABLE OF THE QUALITY METRICS GAINED WITH DIFFERENT ESTIMATION METHODS FOR THREE LEVELS OF NOISE (SNR).
RESULTS ARE REPORTED FOR THE 2ND SYSTEM APPLIED TO THE FIRST SAR SCENE.
SYSTEM SPECIFICATIONS: RANGE TRIANGULAR SHAPE OF AF $\Psi_R(X_2) = 5$ PIXELS WIDTH; AZIMUTH $|SINC|^2$ SHAPE OF AF $\Psi_A(X_1) = 30$ PIXELS WIDTH.

	Method →	**RASF**			**DEDR**			**FBR**			**RFBR**		
	SNR [dB] →	**15**	**20**	**25**	**15**	**20**	**25**	**15**	**20**	**25**	**15**	**20**	**25**
Metrics	**IOSNR [dB]**	9.42	14.87	19.37	7.83	12.96	17.24	5.92	10.23	15.37	6.23	11.73	15.96
	PIOSNR (%)	77.37	82.74	81.24	79.32	87.74	86.41	97.83	94.28	99.26	96.28	93.29	98.64
	MSF	0.30	0.60	0.70	0.33	0.50	0.60	0.13	0.30	0.20	0.14	0.32	0.24

TABLE 4

COMPARATIVE TABLE OF THE QUALITY METRICS GAINED WITH DIFFERENT ESTIMATION METHODS FOR THREE LEVELS OF NOISE (SNR).
RESULTS ARE REPORTED FOR THE 1ST SYSTEM APPLIED TO THE SECOND SAR SCENE.
SYSTEM SPECIFICATIONS: RANGE TRIANGULAR SHAPE OF AF $\Psi_R(X_2) = 5$ PIXELS WIDTH; AZIMUTH $|SINC|^2$ SHAPE OF AF $\Psi_A(X_1) = 40$ PIXELS WIDTH.

	Method →	**RASF**			**DEDR**			**FBR**			**RFBR**		
	Noise [dB] →	**15**	**20**	**25**	**15**	**20**	**25**	**15**	**20**	**25**	**15**	**20**	**25**
Metrics	**IOSNR [dB]**	12.42	17.82	22.75	9.42	14.72	19.64	5.23	10.22	15.33	6.24	11.25	16.45
	PIOSNR (%)	65.77	70.84	69.96	67.28	75.44	74.43	90.33	87.38	93.70	89.18	86.39	92.54
	MSF	0.26	0.56	0.66	0.29	0.46	0.56	0.14	0.26	0.16	0.10	0.28	0.20

TABLE 5
COMPARATIVE TABLE OF THE QUALITY METRICS GAINED WITH DIFFERENT ESTIMATION METHODS FOR THREE LEVELS OF NOISE (SNR).
RESULTS ARE REPORTED FOR THE 2ND SYSTEM APPLIED TO THE SECOND SAR SCENE.
SYSTEM SPECIFICATIONS: RANGE TRIANGULAR SHAPE OF AF $\Psi_R(X_2) = 5$ PIXELS WIDTH; AZIMUTH $|SINC|^2$ SHAPE OF AF $\Psi_A(X_1) = 50$ PIXELS WIDTH.

	Method →	RASF			DEDR			FBR			RFBR		
	SNR [dB] →	15	20	25	15	20	25	15	20	25	15	20	25
Metrics	IOSNR [dB]	13.64	18.32	23.74	10.45	15.76	20.73	6.37	11.52	16.75	7.43	12.53	17.89
	PIOSNR (%)	74.77	79.74	78.42	76.32	84.44	83.41	94.63	91.53	97.12	93.58	90.89	96.74
	MSF	0.25	0.55	0.65	0.28	0.45	0.55	0.08	0.25	0.15	0.09	0.27	0.19

TABLE 6
NUMBER OF OPERATIONS PER CYCLE FOR COMPUTATIONAL IMPLEMENTATION OF DIFFERENT ENHANCED IMAGING METHODS.
RESULTS ARE REPORTED FOR EACH ANALYZED METHOD.

Method	Equation	Processing Algorithm		Operations per cycle
DEDR	(24)	$\mathbf{F}_{DEDR} = \mathbf{K}_{\mathbf{A},\alpha,\beta}\mathbf{S}^{+}\mathbf{R}_{\Sigma}^{-1}$	→	$K^{(2)} \cdot I$
FBR	(31)	$\hat{\mathbf{B}}_{FBR} = \mathbf{B}_P + \mathbf{P}\mathbf{B}_0 + \mathbf{W}(\hat{\mathbf{B}})\{\mathbf{V}(\hat{\mathbf{B}}) - \mathbf{Z}(\hat{\mathbf{B}})\}$	→	$K + K^{(2)} + K^{(4)} \cdot I$
RFBR	(34)	$\hat{\mathbf{B}}_{RFBR} = \mathbf{B}_0 + \mathbf{\Omega V}$	→	$K + K^{(2)} \cdot I$
MSF	(36)	$\hat{\mathbf{B}}_{MSF} = \mathbf{\Omega \Pi}$	→	$K \cdot I$
RASF	(37)	$\mathbf{F}_{RASF} = (\mathbf{S}^{+}\mathbf{R}_{\mathbf{N}}^{-1}\mathbf{S} + \hat{\mathbf{D}}^{-1})^{-1}\mathbf{S}^{+}\mathbf{R}_{\mathbf{N}}^{-1}$	→	$K \cdot I^{(2)}$

TABLE 7
COMPARATIVE TABLE OF THE REQUIRED PROCESSING TIME FOR THE COMPARED ENHANCED IMAGING METHODS.
THE RESULTS ARE REPORTED IN SECONDS.
NOTE – PROCESSING TIMES ARE CALCULATED CONSIDERING ALL THE CPU CLOCK SPEED IS DEDICATED;
RESULTS MAY VARY DEPENDING ON THE PROCESSOR TYPE, CPU MEMORY AND SOFTWARE USED.

Method	Operation per cycle	Total operations	PC Time [seconds]	WS Time [seconds]	DH Time [seconds]
DEDR	$K^{(2)} \cdot I$	1.34×10^{8}	0.05	0.035	0.45
FBR	$K + K^{(2)} + K^{(4)} \cdot I$	3.48×10^{13}	1.30×10^{4}	9.15×10^{3}	11.60×10^{3}
RFBR	$K + K^{(2)} \cdot I$	6.92×10^{10}	26.15	18.21	230.66
MSF	$K \cdot I$	1.34×10^{8}	0.05	0.035	0.45
ASF	$K \cdot I^{(2)}$	6.76×10^{10}	25.41	17.69	225.12

VII. CONCLUDING REMARKS

We have performed the detailed comparative study of different proposed robust numerical versions of two recently developed high-resolution adaptive radar/SAR imaging methodologies: DEDR and FBR techniques. The undergone study revealed structural similarity of the robustified algorithms invoked from both methodologies, in particular, structural similarity of the RASF (DEDR-related) and the RFBR (robust FBR-related) methods. The performed comparative analysis of the computational complexities of different imaging techniques based on the robust SSP and RSS estimators revealed that the DEDR-related and FBR-related robust imaging algorithms manifest user-controlled real-time implementation performances because the RS deadline event is completed in each stage of the image reconstruction process to provide the system response in a virtually "real" (i.e., user-required) time.

In the RS applications related to the real-world 512×512-pixel scene image enhancement/reconstruction scenarios, the computational complexity for performing the enhanced RS imaging with the proposed RFBR algorithm in comparison with the original FBR method was drastically decreased, i.e., approximately 10^5 times and required 27 seconds of the overall computational time. In the same manner, the computation time required for performing the DEDR-related robust RASF imaging algorithm was decreased even more

drastically, approximately 10^{15} times with respect to the adaptive (non-robust) original FBR method and required approximately only 0.50 seconds of the overall computational time. Also, the simulation protocols reported for different testes scenarios verify in more details the substantial efficiency of the proposed here high-resolution robust radar/SAR imaging techniques.

REFERENCES

[1] P.M. Mather, *Computer processing of remotely-sensed images*, John Wiley & Sons, U.S.A., 2004.

[2] E. Schrödinger, *Science, theory and man*, Dover, U.S.A., 1957.

[3] S. Greenfield, *The human brain: a guided tour*, Weinfeld and Nicholson, U.K., 1997.

[4] T. Freeman, Jet Propulsion Laboratory, Space Imaging, "What is imaging radar?", 2005, http://www.spaceimaging.com.

[5] C. Olmsted, *Scientific SAR user's guide*, Alaska SAR Facility, U.S.A. 1993.

[6] Y.V. Shkvarko, "Estimation of Wavefield Power Distribution in the Remotely Sensed Environment: Bayesian Maximum Entropy Approach", *IEEE Transactions on Signal Processing*, vol. 50, pp. 2333-2346, September 2002.

[7] Y.V. Shkvarko, "Unifying Regularization and Bayesian Estimation Methods for Enhanced Imaging with Remotely Sensed Data. Part I – Theory", *IEEE Transactions on Geoscience and Remote Sensing*, vol. 42, pp. 923-931, March 2004.

[8] Y.V. Shkvarko, "Unifying Regularization and Bayesian Estimation Methods for Enhanced Imaging with Remotely Sensed Data. Part II – Implementation and Performance Issues", *IEEE Transactions on Geoscience and Remote Sensing*, vol. 42, pp. 932-940 , March 2004.

[9] F.M. Henderson and A.V. Lewis, *Principles and application of imaging radar, manual of remote sensing*, John Wiley & Sons, U.S.A., 1998.

[10] J.L. Starck, F. Murtagh and A. Bijaoui, *Image processing and data analysis, the multiscale approach*, Cambridge University Press, U.K., 1998.

[11] B.R. Mahafza, *Radar systems analysis and design using MATLAB*, CRC Press, U.S.A., 2000.

[12] A.W. Doerry, F.M. Dickey, L.A. Romero and J.M. DeLaurentis, "Difficulties in Superresolving SAR Images", *SPIE Proceedings*, vol. 4727, pp. 122-133, April 2002.

[13] R.C. Puetter, "Information Language and Pixon-based Image Reconstruction", *SPIE Proceedings*, vol. 2827, pp. 12-31, 1996.

[14] S. Haykin and A. Steinhardt, *Adaptive radar detection and estimation*, John Wiley & Sons, U.S.A., 1992.

[15] D.C. Bell and R.M. Narayanan, "Theoretical Aspects of Radar Imaging using Stochastic Waveforms", *IEEE Transactions on Signal Processing*, vol. 49, pp. 349-400, February 2001.

[16] Y.V. Shkvarko, "Theoretical Aspects of Array Radar Imaging via Fusing Experiment Design and Descriptive Regularization Techniques", *Proceedings of the* 2nd *IEEE Workshop on Sensor Array and Multichannel Signal Processing*, Washington U.S.A., 2002.

[17] Space Imaging, 2006, http://www.spaceimaging.com.

[18] R.O. Harger, *Synthetic aperture radar systems: theory and design*, Academic Press, U.S.A. 1970.

[19] R. Bamler, "A Comparison of Range-Doppler and Wave-Number Domain SAR Focusing Algorithms", *IEEE Transactions on Geoscience and Remote Sensing*, vol. 30, pp. 706-713 , June 1991.

[20] S.E. Falkovich, V.I. Ponomaryov and Y.V. Shkvarko, *Optimal spatial-temporal signal processing for spread radio channels*, Radio and Communication Press, USSR 1989.

[21] G. Franceschetti and R. Lanari, *Synthetic aperture radar processing*, Boca Raton, FL:CRC, 1999.

[22] S.A. Hovanessian, *Introduction to sensor systems*, Norwood, MA: Artech House, 1988.

[23] L.G. Cutrona, "Synthetic Aperture Radar", in *Radar handbook*, McGraw-Hill, 1990.

[24] D.R. Wehner, *High-resolution radar*, Artech House, 1994.

[25] Yuriy Shkvarko and Ivan Villalon-Turrubiates, "Remote Sensing Imagery and Signature Fields Reconstruction via Aggregation of Robust Regularization with Neural Computing", in *Advanced Concepts for Intelligent Vision Systems*, J. Blanc-Talon, W. Philips, D. Popescu and P. Scheunders, Ed. Germany: Springer-Verlag, pp. 865-876, August 2007.

[26] Yuriy V. Shkvarko, "Finite Array Observations-Adapted Regularization Unified with Descriptive Experiment Design Approach for High-Resolution Spatial Power Spectrum Estimation with Application to Radar/SAR Imaging", in *Proceedings of the 15nd International Conference on Digital Signal Processing*, Cardiff U.K., July 2007.

[27] Yuriy V. Shkvarko, Ivan E. Villalon-Turrubiates and Jose L. Leyva-Montiel, "Remote Sensing Signature Fields Reconstruction via Robust Regularization of Bayesian Minimum Risk Technique", in *Proceedings of the 2nd IEEE International Workshop on Computational Advances in Multi-Sensor adaptive processing*, Virgin Islands U.S.A., pp. 237-240, December 2007.

Ivan E. Villalon-Turrubiates (M'04) was born in Salamanca Mexico in 1976. He received the Title of Mechanical Engineer in 2000 and the Master of Sciences Degree in Electrical Engineering (Digital Signal Processing) in 2005, both from the University of Guanajuato in Salamanca Mexico. He received the Doctor in Sciences Degree in Electrical Engineering (Digital Signal and Image Processing) in 2007 from the Center for Advanced Research and Education (CINVESTAV) of the National Polytechnic Institute (IPN) of Mexico in Guadalajara.

Presently, he is with the Department of Computer Sciences at the University of Guadalajara, Campus Valles in Ameca, Mexico, with a full-time Professor/Researcher position. Also, he is contributing with the Department of Physical Sciences at the TecMilenio University in Guadalajara, Mexico. His research activities are in applications of signal processing to remote sensing and imaging radar with emphasis in digital applications of signal and image processing in bioengineering. He published two papers in international journals, 2 chapters in scientific books, and 17 articles in international scientific conferences on these topics.

Yuriy V. Shkvarko (SM'05) received the Dip.Eng. (Hon.) degree in radio engineering, the Cand.Sci. degree (Ph.D. equivalent) in radio systems, and the Dr.Sci. degree in radio physics, radar, and Navigation, all from the Kharkov Aviation Institute, Ukraine, in 1976, 1980, and 1990, respectively.

From 1976 to 1991, he was with the Scientific Research Department, Kharkov Aviation Institute, Kharkov, as a Research Fellow, Senior Fellow, and finally as a Chair of the Research Laboratory in information technologies for radar and navigation. From 1991 to 1999, he was a Full Professor with the Department of System Analysis and Control, at the Ukrainian National Polytechnic Institute in Kharkov. From 1999 to 2001, he was a Visiting Professor with the Guanajuato University at Salamanca, Mexico. In 2001, he joined the CINVESTAV del IPN, Unidad Guadalajara, Mexico, as a Full Titular Professor. His research interests are in applications of signal processing to remote sensing, imaging radar, navigation, and communications, particularly in inverse problems, random fields estimation, adaptive spatial analysis, statistical sensor array, and multichannel processing, and system fusion. He holds 12 patents and has published two books and some 130 papers in journals and conference records on these topics.